WIND ENERGY
Wind Energ. 2012; **00**:1–20
DOI: 10.1002/we

RESEARCH ARTICLE

Finite element simulation of wind turbine aerodynamics: Validation study using NREL Phase VI experiment

Ming-Chen Hsu, Ido Akkerman and Yuri Bazilevs

Department of Structural Engineering, University of California, San Diego, 9500 Gilman Drive, La Jolla, CA 92093, USA

ABSTRACT

A validation study using the NREL Phase VI wind turbine is presented. The aerodynamics simulations are performed using the finite element ALE–VMS formulation augmented with weakly enforced essential boundary conditions. In all cases the rotor is assumed to be rigid and its rotation is prescribed. The rotor-only simulations are performed for a wide range of wind conditions and the computational results compare favorably with the experimental findings in all cases. The sliding-interface method is adopted for the simulation of the full wind turbine configuration. The full-wind-turbine simulations capture the blade–tower interaction effect, and the results of these simulations are also in good agreement with the experimental data.

KEYWORDS

NREL Phase VI; wind turbine aerodynamics; ALE–VMS formulation; finite element method; sliding-interface method; blade–tower interaction

Correspondence
Yuri Bazilevs, Department of Structural Engineering, University of California, San Diego, 9500 Gilman Drive, Mail Code 0085, La Jolla, CA 92093, USA.

E-mail: yuri@ucsd.edu

Received . . .

1. INTRODUCTION

As the demands for wind energy grow, the wind energy industry is moving in the direction of very large-scale designs that are expected to reliably operate in a variety of environmental conditions. One such example is floating wind turbines, which are expected to sustain not only increased wind loads, but also loads coming from ocean waves and underwater currents. Such designs may benefit from the use of high-fidelity computational methods that incorporate 3D geometry, time dependence, and interaction between multiple physical systems without the inherent empiricism present in low-fidelity techniques. Accurate prediction of the aerodynamics, hydrodynamics, and structural behavior of wind turbines at full scale is even more critical in such cases in order to create reliable and efficient designs. The reliability and efficiency of the design directly translate into lower energy costs.

In recent years, there has been a growing body of research and development to raise the fidelity and predictive power of wind turbine simulations. These include standalone 3D computational fluid dynamics (CFD) simulations of wind turbines with a variety of methods [1–13], and standalone structural analyses of rotor blades of complex geometry and material composition under assumed or computed off-line wind load conditions [14–20]. A fully coupled fluid–structure interaction (FSI) simulation methodology for wind turbine rotors was developed by Bazilevs *et al.* [21]. The simulations therein showed the importance of FSI modeling for full-scale wind turbine rotors.

While most of the CFD work on wind turbine aerodynamics is based on finite volume or finite difference discretizations, in our earlier work [7, 8, 21, 22] we opt for numerical methods that are based on the weak or variational forms of the governing equations, such as the finite element method (FEM) or Isogeometric Analysis (IGA) [23, 24]. The latter is an alternative method to the FEM, which makes use of higher-order, smooth basis functions emanating from the fields of computer-aided design and computer graphics. The choice of the variational approach is based on several considerations, the two of which are: 1. It enables the formulation of novel, multiscale turbulence modeling approaches [25–28], which

do not rely on the empiricism of eddy-viscosity methods; 2. The coupling with structural mechanics (typically computed with FEM or IGA) for the purposes of FSI modeling is greatly simplified.

In this paper, we perform an extensive validation study in which we compare our aerodynamics simulation results with the data of the experiments performed on the NREL Phase VI wind turbine [29, 30]. In these simulations, only the rotor is modeled and the effect of the tower and other wind turbine components is neglected.

In simulating wind turbine aerodynamics, only a handful of researchers (see, e.g., Gómez-Iradi *et al.* [5], Zahle *et al.* [6], and Li *et al.* [10]) considered full wind turbine simulations, where the rotating wind turbine rotor and stationary nacelle and tower are all modeled. This is because of the additional numerical challenges associated with the simulation of objects in relative motion. In this paper we adopt a sliding-interface formulation, first proposed by Bazilevs and Hughes [31] and suitable for the FEM or IGA discretizations, to address the above challenges. Full-wind-turbine computations are also performed using the sliding-interface method, and the result are compared to the rotor-only simulations and the experimental data. The experimental data indicates that in some cases the tower produces an appreciable effect on the blade aerodynamic loads. We note that in application of the FEM to flows with moving mechanical components, the Shear–Slip Mesh Update Method (SSMUM) [32–34] may also be employed to handle objects in relative motion.

This paper is outlined as follows. In Section 2, we introduce the arbitrary Lagrangian–Eulerian (ALE) form of the Navier–Stokes equations of incompressible flow suitable for moving domain problems. We also present the residual-based variational multiscale (VMS) formulation of the Navier–Stokes equations and turbulence modeling [25], which we refer to as the ALE–VMS method. The ALE–VMS formulation is augmented with weakly enforced essential boundary conditions [26–28, 35], which improve the accuracy of the simulations of flows with thin turbulent boundary layers. In Section 3, we present the rotor-only simulation results for the NREL Phase VI wind turbine. For all cases considered, very good agreement with the experimental data is obtained for the low-speed shaft torque, root flap bending moment, force coefficients and pressure distribution on the blade axial cross-sections. In Section 4, we present the sliding-interface method, which handles the relative motion between the rotor and the rest of the wind turbine. We apply the method to simulate the full wind turbine configuration and study the effect of blade–tower interaction. The simulation results likewise compare favorably with the experimental data. In Section 5, we draw conclusions and outline future developments.

2. CONTINUUM AND DISCRETE MODELING OF WIND TURBINE AERODYNAMICS

The wind turbine aerodynamics is governed by the Navier–Stokes equations of incompressible flow posed on a moving domain. The domain motion is handled using the arbitrary Lagrangian–Eulerian (ALE) framework [36]. Although aerodynamic phenomena are generally described using the Navier–Stokes equations of compressible flow, the incompressible-flow assumption is valid for the present application where the Mach number is typically low*.

2.1. Continuous problem

In what follows, $\Omega_t \in \mathbb{R}^d$, $d = 2, 3$, denotes the spatial domain of the aerodynamics problem with boundary Γ_t at time $t \in (0, T)$. The subscript t indicates that the fluid mechanics spatial domain is time-dependent. The Navier–Stokes equations of incompressible flow in the ALE form may be written on Ω_t and $\forall t \in (0, T)$ as

$$\begin{aligned} \rho\left(\left.\frac{\partial \mathbf{u}}{\partial t}\right|_{\hat{x}} + (\mathbf{u}-\hat{\mathbf{u}})\cdot\nabla\mathbf{u} - \mathbf{f}\right) - \nabla\cdot\boldsymbol{\sigma} &= \mathbf{0}, \\ \nabla\cdot\mathbf{u} &= 0, \end{aligned} \tag{1}$$

where ρ is the density of the fluid, $\mathbf{u}$ is the velocity, $\hat{\mathbf{u}}$ is the velocity of the fluid domain Ω_t, $\mathbf{f}$ is the external force (per unit mass), and $\boldsymbol{\sigma}$ is the stress tensor defined as

$$\boldsymbol{\sigma}(\mathbf{u}, p) = -p\mathbf{I} + 2\mu\boldsymbol{\varepsilon}(\mathbf{u}). \tag{2}$$

Here p is the pressure, $\mathbf{I}$ is the identity tensor, μ is the dynamic viscosity, and $\boldsymbol{\varepsilon}(\mathbf{u})$ is the strain-rate tensor given by

$$\boldsymbol{\varepsilon}(\mathbf{u}) = \frac{1}{2}\left(\nabla\mathbf{u} + \nabla\mathbf{u}^T\right). \tag{3}$$

In Eq. (1), $\left|_{\hat{x}}\right.$ denotes the fact that the time derivative is taken with respect to a fixed referential domain spatial coordinates $\hat{\mathbf{x}}$. The spatial gradients ∇ are taken with respect to the spatial coordinates $\mathbf{x}$ of the current configuration.

*For modern, large wind turbines, the Mach number near the blade tips may reach about 0.3, suggesting that compressibility effects may play a small role in this region. However, for the wind turbine considered in this work, the flow can be safely considered incompressible everywhere in the domain.

Wind Energ. 2012; **00**:1–20 © 2012 John Wiley & Sons, Ltd.
DOI: 10.1002/we
Prepared using weauth.cls

2.2. ALE–VMS formulation with weakly enforced boundary conditions

We assume that the time-dependent fluid domain Ω_t is divided into N_{el} individual spatial finite element subdomains denoted by Ω_t^e. The boundary $(\Gamma_t)_{\text{g}}$ is decomposed into N_{eb} surface elements denoted by Γ_t^b. The trial function spaces $\mathcal{S}_u^h$ for the velocity and $\mathcal{S}_p^h$ for the pressure, as well as the corresponding test function spaces $\mathcal{V}_u^h$ and $\mathcal{V}_p^h$ are assumed to be comprised of piece-wise linear finite element functions. Equal order interpolation of the velocity and pressure is employed in this work.

The finite element ALE–VMS formulation of aerodynamics, based on the Navier–Stokes equations of incompressible flow, and including weakly enforced essential boundary conditions, is given by: find $\mathbf{u}^h \in \mathcal{S}_u^h$ and $p^h \in \mathcal{S}_p^h$, such that, $\forall \mathbf{w}^h \in \mathcal{V}_u^h$ and $q^h \in \mathcal{V}_p^h$

$$B^{VMS}(\{\mathbf{w}^h, q^h\}, \{\mathbf{u}^h, p^h\}; \hat{\mathbf{u}}^h) + B^{WBC}(\{\mathbf{w}^h, q^h\}, \{\mathbf{u}^h, p^h\}; \hat{\mathbf{u}}^h) - F(\{\mathbf{w}^h, q^h\}) = 0, \tag{4}$$

where

$$\begin{aligned} B^{VMS}(\{\mathbf{w}^h, q^h\}, \{\mathbf{u}^h, p^h\}; \hat{\mathbf{u}}^h) = & \int_{\Omega_t} \mathbf{w}^h \cdot \rho \left(\left. \frac{\partial \mathbf{u}^h}{\partial t} \right|_{\hat{x}} + \left(\mathbf{u}^h - \hat{\mathbf{u}}^h\right) \cdot \boldsymbol{\nabla} \mathbf{u}^h \right) \mathrm{d}\Omega \\ & + \int_{\Omega_t} \boldsymbol{\varepsilon}\left(\mathbf{w}^h\right) : \boldsymbol{\sigma}\left(\mathbf{u}^h, p^h\right) \mathrm{d}\Omega + \int_{\Omega_t} q^h \boldsymbol{\nabla} \cdot \mathbf{u}^h \, \mathrm{d}\Omega \\ & + \sum_{e=1}^{N_{\text{el}}} \int_{\Omega_t^e} \tau_{\text{SUPS}} \left(\left(\mathbf{u}^h - \hat{\mathbf{u}}^h\right) \cdot \boldsymbol{\nabla} \mathbf{w}^h + \frac{\boldsymbol{\nabla} q^h}{\rho} \right) \cdot \mathbf{r}_{\text{M}}\left(\mathbf{u}^h, p^h\right) \mathrm{d}\Omega \\ & + \sum_{e=1}^{N_{\text{el}}} \int_{\Omega_t^e} \rho \nu_{\text{LSIC}} \boldsymbol{\nabla} \cdot \mathbf{w}^h r_{\text{C}}(\mathbf{u}^h) \, \mathrm{d}\Omega \\ & - \sum_{e=1}^{N_{\text{el}}} \int_{\Omega_t^e} \tau_{\text{SUPS}} \mathbf{w}^h \cdot \left(\mathbf{r}_{\text{M}}\left(\mathbf{u}^h, p^h\right) \cdot \boldsymbol{\nabla} \mathbf{u}^h \right) \mathrm{d}\Omega \\ & - \sum_{e=1}^{N_{\text{el}}} \int_{\Omega_t^e} \frac{\boldsymbol{\nabla} \mathbf{w}^h}{\rho} : \left(\tau_{\text{SUPS}} \mathbf{r}_{\text{M}}\left(\mathbf{u}^h, p^h\right) \right) \otimes \left(\tau_{\text{SUPS}} \mathbf{r}_{\text{M}}\left(\mathbf{u}^h, p^h\right) \right) \mathrm{d}\Omega, \end{aligned} \tag{5}$$

$$\begin{aligned} B^{WBC}(\{\mathbf{w}^h, q^h\}, \{\mathbf{u}^h, p^h\}; \hat{\mathbf{u}}^h) = & - \sum_{b=1}^{N_{\text{eb}}} \int_{\Gamma_t^b \cap (\Gamma_t)_{\text{g}}} \mathbf{w}^h \cdot \boldsymbol{\sigma}\left(\mathbf{u}^h, p^h\right) \mathbf{n} \, \mathrm{d}\Gamma \\ & - \sum_{b=1}^{N_{\text{eb}}} \int_{\Gamma_t^b \cap (\Gamma_t)_{\text{g}}} \left(2\mu \boldsymbol{\varepsilon}\left(\mathbf{w}^h\right) \mathbf{n} + q^h \mathbf{n} \right) \cdot \left(\mathbf{u}^h - \mathbf{g}\right) \mathrm{d}\Gamma \\ & - \sum_{b=1}^{N_{\text{eb}}} \int_{\Gamma_t^b \cap (\Gamma_t)_{\text{g}}^-} \mathbf{w}^h \cdot \rho \left(\left(\mathbf{u}^h - \hat{\mathbf{u}}^h\right) \cdot \mathbf{n} \right) \left(\mathbf{u}^h - \mathbf{g}\right) \mathrm{d}\Gamma \\ & + \sum_{b=1}^{N_{\text{eb}}} \int_{\Gamma_t^b \cap (\Gamma_t)_{\text{g}}} \tau_{\text{B}} \mathbf{w}^h \cdot \left(\mathbf{u}^h - \mathbf{g}\right) \mathrm{d}\Gamma, \end{aligned} \tag{6}$$

and

$$F(\{\mathbf{w}^h, q^h\}) = \int_{\Omega_t} \mathbf{w}^h \cdot \rho \mathbf{f} \, \mathrm{d}\Omega + \int_{(\Gamma_t)_{\text{h}}} \mathbf{w}^h \cdot \mathbf{h} \, \mathrm{d}\Gamma. \tag{7}$$

In the above formulation the ALE method is employed to handle the moving spatial domain problem. The discrete velocities and pressures and the corresponding test functions are superscripted with h to denote their dependence on the mesh size. In Eqs. (4)–(7), $\hat{\mathbf{u}}^h$ is the mesh velocity, $\mathbf{h}$ is the prescribed traction boundary condition on $(\Gamma_t)_{\text{h}}$, $\mathbf{n}$ is the outward wall-normal unit vector, $(\Gamma_t)_{\text{g}}$ is the part of the boundary where the velocity boundary condition $\mathbf{g}$ is set, and $(\Gamma_t)_{\text{g}}^-$ is defined as the "inflow" part of $(\Gamma_t)_{\text{g}}$:

$$(\Gamma_t)_{\text{g}}^- = \left\{ \mathbf{x} \;\middle|\; \left(\mathbf{u}^h - \hat{\mathbf{u}}^h\right) \cdot \mathbf{n} < 0, \; \forall \mathbf{x} \subset (\Gamma_t)_{\text{g}} \right\}. \tag{8}$$

If $(\Gamma_t)_{\text{g}}$ coincides with the moving wall (rigid or flexible), then $\mathbf{g}$ is the prescribed wall velocity. In Eq. (5), $\mathbf{r}_{\text{M}}$ and r_{C} are the residuals of the momentum and continuity (incompressibility constraint) equations, respectively, given by

$$\mathbf{r}_{\text{M}}(\mathbf{u}^h, p^h) = \rho \left(\left. \frac{\partial \mathbf{u}^h}{\partial t} \right|_{\hat{x}} + \left(\mathbf{u}^h - \hat{\mathbf{u}}^h\right) \cdot \boldsymbol{\nabla} \mathbf{u}^h - \mathbf{f} \right) - \boldsymbol{\nabla} \cdot \boldsymbol{\sigma}\left(\mathbf{u}^h, p^h\right), \tag{9}$$

and

$$r_C(\mathbf{u}^h) = \boldsymbol{\nabla} \cdot \mathbf{u}^h, \tag{10}$$

and τ_{SUPS} and ν_{LSIC} are the stabilization parameters defined as

$$\tau_{\text{SUPS}} = \left(\frac{4}{\Delta t^2} + \left(\mathbf{u}^h - \hat{\mathbf{u}}^h\right) \cdot \mathbf{G} \left(\mathbf{u}^h - \hat{\mathbf{u}}^h\right) + C_I \nu^2 \mathbf{G} : \mathbf{G} \right)^{-1/2}, \tag{11}$$

and

$$\nu_{\text{LSIC}} = (\text{tr}\mathbf{G}\ \tilde{\tau}_{\text{SUPS}})^{-1}, \tag{12}$$

where

$$\tilde{\tau}_{\text{SUPS}} = \left(\left(\mathbf{u}^h - \hat{\mathbf{u}}^h\right) \cdot \mathbf{G} \left(\mathbf{u}^h - \hat{\mathbf{u}}^h\right) + C_I \nu^2 \mathbf{G} : \mathbf{G} \right)^{-1/2}. \tag{13}$$

Here, Δt is the time-step size, $\nu = \mu/\rho$ is the kinematic viscosity, $\mathbf{G}$ is the element metric tensor defined as

$$G_{ij} = \sum_{k=1}^{d} \frac{\partial \xi_k}{\partial x_i} \frac{\partial \xi_k}{\partial x_j}, \tag{14}$$

where $\partial \boldsymbol{\xi}/\partial \mathbf{x}$ is the inverse Jacobian of the element mapping between the parametric and physical domain, tr$\mathbf{G}$ is the trace of $\mathbf{G}$, and C_I is a positive constant, independent of the mesh size, derived from an appropriate element-wise inverse estimate [37–39].

Remark 1. The stabilization parameters τ_{SUPS} and ν_{LSIC} in the above equations originate from stabilized finite element methods for fluid dynamics [25, 40–48]. They were designed such that optimal convergence with respect to the mesh size and polynomial order of discretization is attained for linear model problems of direct relevance to fluid mechanics (see Hughes *et al.* [46] and references therein). Furthermore, enhanced stability for advection-dominated flows and the ability to conveniently employ the same basis functions for velocity and pressure variables for incompressible flow are some of the attractive outcomes of this method. More recently, the stabilization parameters were derived in the context of the variational multiscale (VMS) methods [49, 50] and were interpreted as the appropriate averages of the small-scale Green's function [51]. The ALE–VMS formulation is a moving-domain extension of the residual-based variational multiscale (RBVMS) turbulence modeling technique proposed by Bazilevs *et al.* [25] for stationary-domain problem. It was also presented in Bazilevs *et al.* [47] for moving domains in the context of FSI. Recently, Takizawa and Tezduyar [52] extended

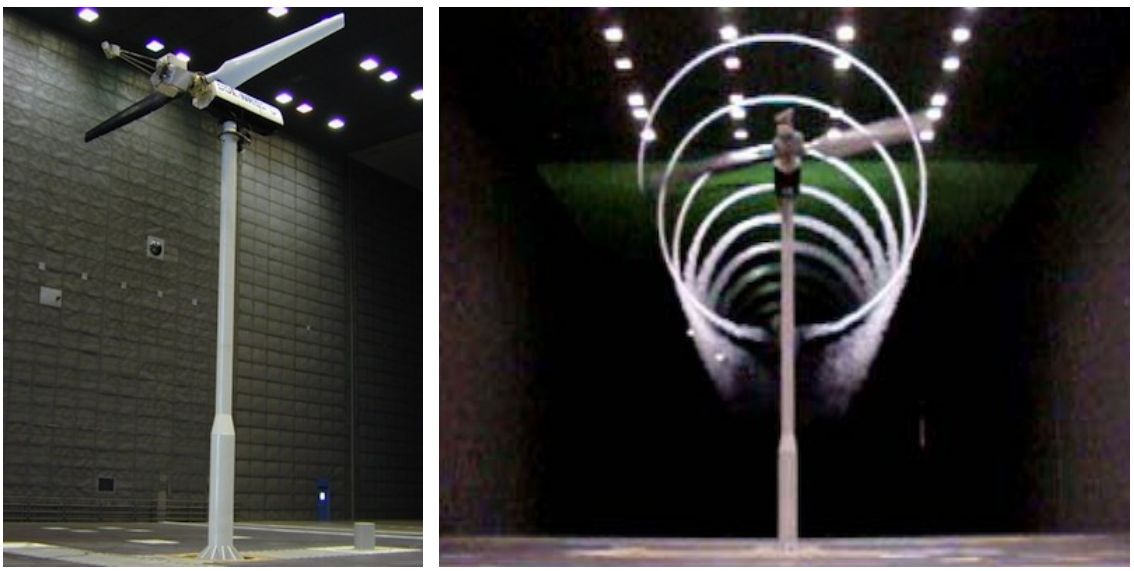

(a) (b)

Figure 1. (a) NREL UAE Phase VI wind turbine in the NASA Ames 80 ft × 120 ft wind tunnel. (b) Wake flow visualization of the operating turbine in the wind tunnel. The images are taken from Hand *et al.* [29].

Wind Energ. 2012; **00**:1–20 © 2012 John Wiley & Sons, Ltd.
DOI: 10.1002/we
Prepared using weauth.cls

the RBVMS formulation for moving domain problems using the space–time finite element method. Note that, in contrast to classical turbulence modeling approaches, no ad hoc eddy viscosity terms are present in the RBVMS or ALE–VMS formulation, which is one of its distinguishing features.

The terms given by Eq. (6) are responsible for weak enforcement of essential boundary conditions (i.e., the velocity boundary conditions). The method of weak enforcement of essential boundary conditions was first proposed in Bazilevs and Hughes [35] and further refined in Bazilevs *et al.* [26–28]. The main advantage of this method over the standard strongly enforced boundary condition approach, in which the nodal solution at the boundary is overwritten with the known prescribed boundary condition, is the added flexibility to allow the flow to slip on the solid surface in the case when the wall-normal mesh size is relatively large. This effect tends to produce more accurate fluid mechanics solutions than those coming from strongly enforced boundary conditions when the boundary-layer mesh is not sufficiently fine to resolve the detailed turbulent flow features. The importance of employing weakly enforced boundary conditions for predicting wind turbine aerodynamics using the ALE–VMS methodology was shown in Hsu *et al.* [53].

In Eq. (6), the parameter τ_{B} is defined as

$$\tau_{\text{B}} = \frac{C_I^B \mu}{h_n}, \tag{15}$$

where h_n is the wall-normal element size, and C_I^B is a sufficiently large positive constant, which is computed from an appropriate element-level inverse estimate [37–39]. The definition given by Eq. (15) ensures that the weak boundary condition formulation is numerically stable.

Remark 2. Rather than setting the no-slip boundary conditions exactly, the weak boundary condition formulation gives the no-slip solution only in the limit as $h_n \to 0$. Note that, when the mesh is refined to capture the boundary layer, the weak boundary condition formulation converges to the strong boundary condition solution (see Bazilevs *et al.* [26]).

Remark 3. Applying global force and moment conservation arguments to the weak boundary condition formulation, Bazilevs and Akkerman [28] derived a so-called conservative definition of the aerodynamic traction vector:

$$\mathbf{h}^h = -p^h \mathbf{n} + 2\mu\boldsymbol{\varepsilon}\left(\mathbf{u}^h\right)\mathbf{n} - \tau_{\text{B}}\left(\mathbf{u}^h - \mathbf{g}\right). \tag{16}$$

The computation of all rotor forces and moments in this paper is based on this definition, which, besides the usual pressure and viscous traction contributions, contains terms pertaining to the lack of strong enforcement of the no-slip boundary conditions. Note that, as the mesh is refined, and better satisfaction of the no-slip condition is achieved, the above definition reverts to the classical one.

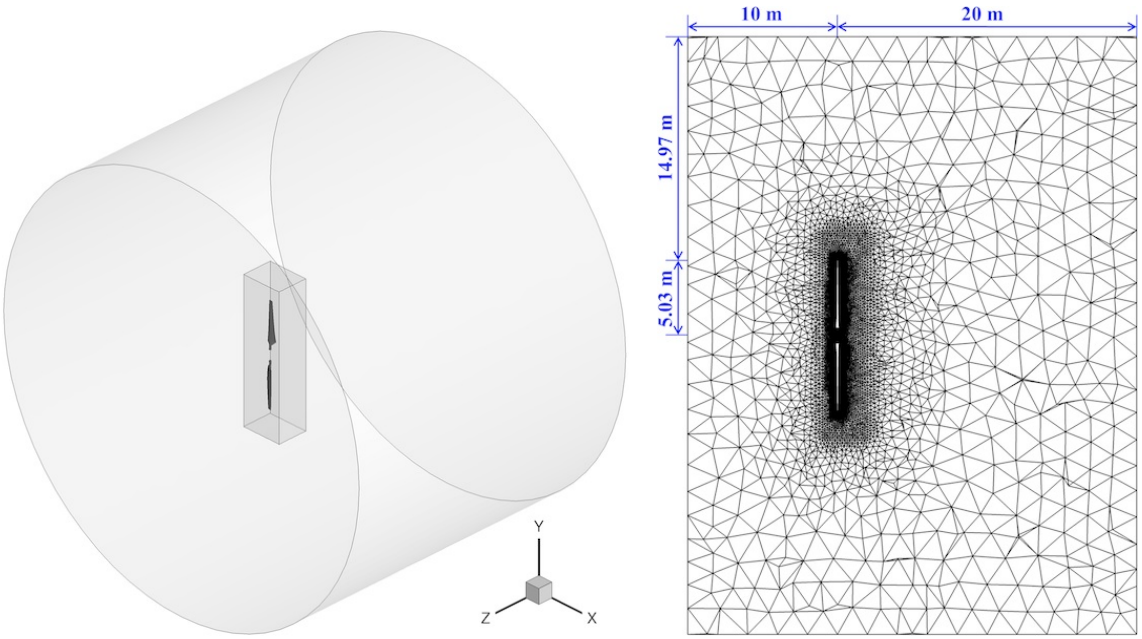

Figure 2. The computational domain and problem mesh. The mesh is refined in the inner region for better flow resolution near the rotor.

Table I. Selected blade cross-section geometry data for the NREL UAE Phase VI rotor. For the complete table, see Hand *et al.* [29] and Jonkman [54].

Radial Distance r (m)	Span Station (r/5.029 m)	Chord Length (m)	Twist (degrees)	Twist Axis (% chord)	Airfoil (-)
0.508	0.100	0.218	0.0	50	Cylinder
1.510	0.300	0.711	14.292	30	NREL S809
2.343	0.466	0.627	4.715	30	NREL S809
3.185	0.633	0.542	1.115	30	NREL S809
4.023	0.800	0.457	-0.381	30	NREL S809
4.780	0.950	0.381	-1.469	30	NREL S809
5.029	1.000	0.355	-1.815	30	NREL S809

3. COMPUTATIONAL RESULTS

3.1. NREL Unsteady Aerodynamics Experiment Phase VI

To assess the accuracy of the ALE–VMS methodology in predicting wind turbine aerodynamics, we perform a validation study where we simulate the NREL Unsteady Aerodynamics Experiment (UAE) Phase VI wind turbine [29], and compare our results with the existing experimental data for this case. This two-bladed experimental wind turbine has a rotor diameter of 10.058 m, hub height of 12.192 m, and a rated power of 19.8 kW. It was tested in the wind tunnel at NASA Ames, and is considered to be one of the most comprehensive, accurate, and reliable experiments carried out on a full-scale wind turbine (see Figure 1). The measured quantities were studied by many computational researchers [1–6, 10, 53–60] for the purposes of validating their simulation software and improving their ability to predict wind turbine aerodynamics. The Phase VI rotor geometry makes use of a single NREL S809 airfoil [61]. Selected blade cross-section geometry data are summarized in Table I, and the detailed documentation of the rotor configuration and its technical specifications are available in Hand *et al.* [29]. For this validation study, wind speeds of 5, 7, 10, 15, 20 and 25 m/s were selected from the experimental sequence S. The experimental sequence S setup consists the wind turbine rotor in the upwind configuration, 0° yaw angle, 0° cone angle, rotational speed of 72 rpm, and blade tip pitch angle of 3°.

Figure 2 shows the computational setup and mesh resolution used in this study. The wind turbine rotor radius R is 5.029 m and the blade is assumed to be rigid. The aerodynamic computation with prescribed wind and rotor speeds is carried out on a rotating mesh. The mesh is refined in the inner region for better resolving the flow near the rotor. At the inflow boundary the wind speed is set to 5, 7, 10, 15, 20 or 25 m/s. The traction vector at the outflow boundary and the radial component of the velocity at the radial boundary are set to zero. The air density and viscosity are 1.23 kg/m^3 and 1.78×10^{-5} kg/(m·s), respectively. The mesh is comprised of 3,795,447 linear elements and 1,126,615 nodes. Figure 3 shows a 2D blade cross-section at 80% spanwise station to illustrate the boundary-layer mesh used in the computations. The size of the first element in the wall-normal direction is 0.002 m, and 15 layers of prismatic elements were generated

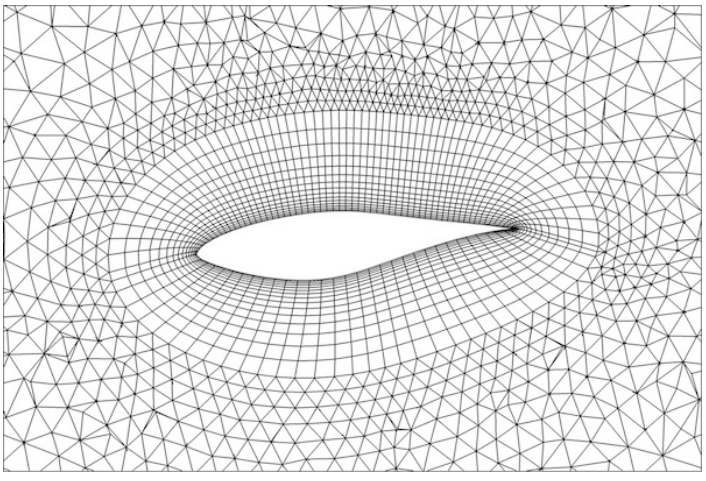

Figure 3. A 2D blade cross-section at $r/R = 80\%$ to illustrate the boundary-layer mesh. The size of the first element in the wall-normal direction is about 0.002 m, and a growth ratio of 1.2 is used to generate 15 layers of prismatic elements.

Wind Energ. 2012; **00**:1–20 © 2012 John Wiley & Sons, Ltd.
DOI: 10.1002/we
Prepared using weauth.cls

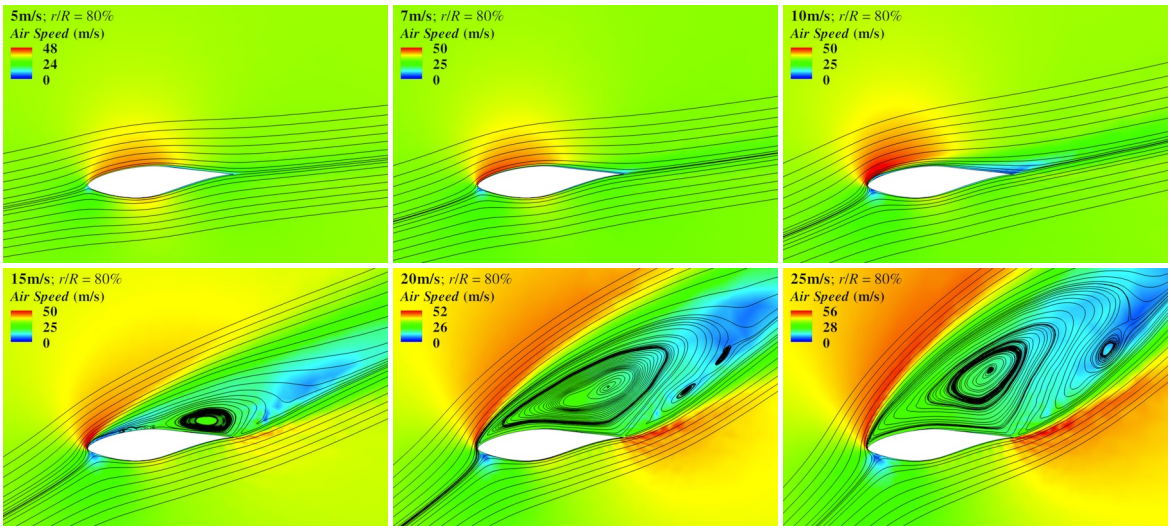

Figure 4. Air speed contours and velocity streamlines at 80% spanwise station for all case.

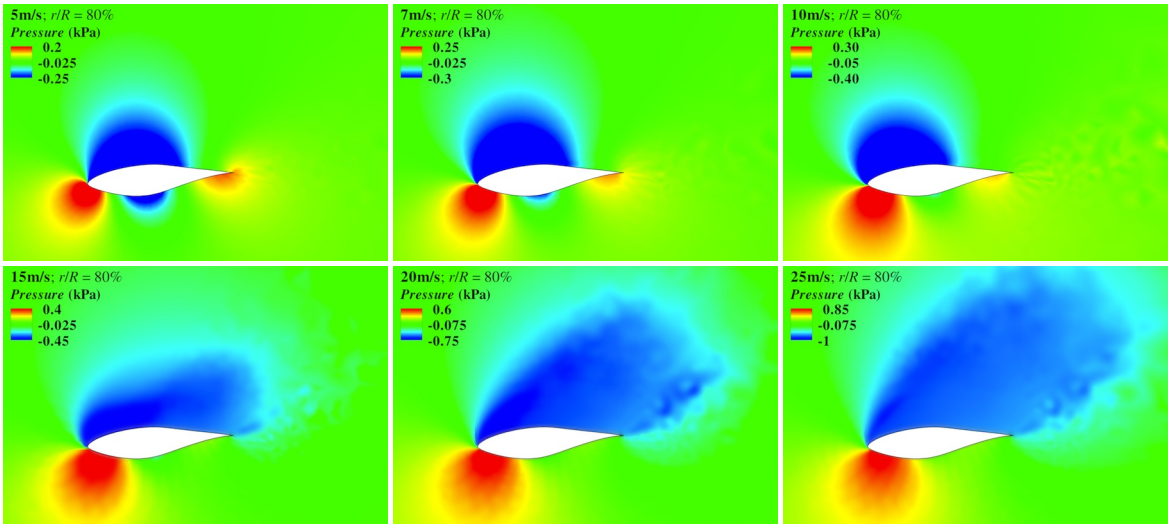

Figure 5. Pressure contours at 80% spanwise station for all cases.

with a growth ratio of 1.2. The Reynolds number based on the chord length and relative speed at this location is $O(10^6)$ and the corresponding y^+ is $O(10^2)$.

The computations were carried out in a parallel computing environment on the Lonestar Linux Cluster at the Texas Advanced Computing Center (TACC) [62]. The system consists of 1,888 compute nodes, each with two Intel Xeon X5680 3.33GHz hex-core processors and 24GB of memory. The mesh is partitioned into 384 subdomains using METIS [63], and each subdomain is assigned to a compute core. The parallel implementation of the methodology and its strong linear scaling can be found in Hsu *et al.* [64].

The ALE–VMS equations are integrated in time using the Generalized-α method [47, 65, 66]. The linear system is solved using a GMRES method [67, 68] with diagonal preconditioning. The time-step size is 1.0×10^{-5} s for 5 to 10 m/s cases, and 5.0×10^{-6} s for the rest of the cases. We typically use three Newton iterations per time step, with 25, 35 and 50 to 100 GMRES iterations for the first, second and third Newton iterations, respectively. With this setup, it takes about six hours to compute 10,000 time steps. All computations are started "impulsively", meaning the initial wind speed in the domain interior is set to that of the inlet, except at the rotor, where it is set to be consistent with the boundary conditions. We usually start collecting time averages of the quantities of interest after two-to-three rotor revolutions. We continue the simulations until the time-averaged value of the aerodynamic torque does not change, which takes no more than another two revolutions.

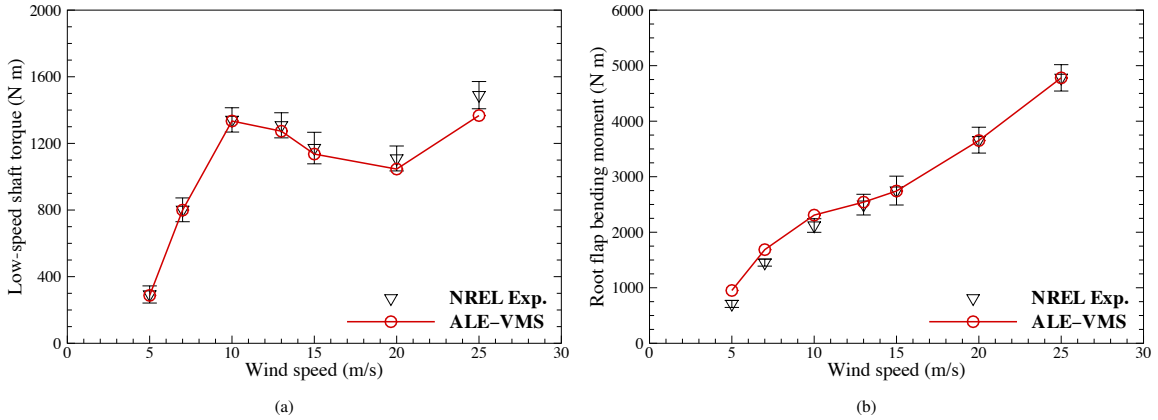

Figure 6. (a) The low-speed shaft (aerodynamic) torque and (b) the root flap bending moment for all cases. The simulation results are compared with the NREL experimental data. The vertical bar represents plus and minus one standard deviation.

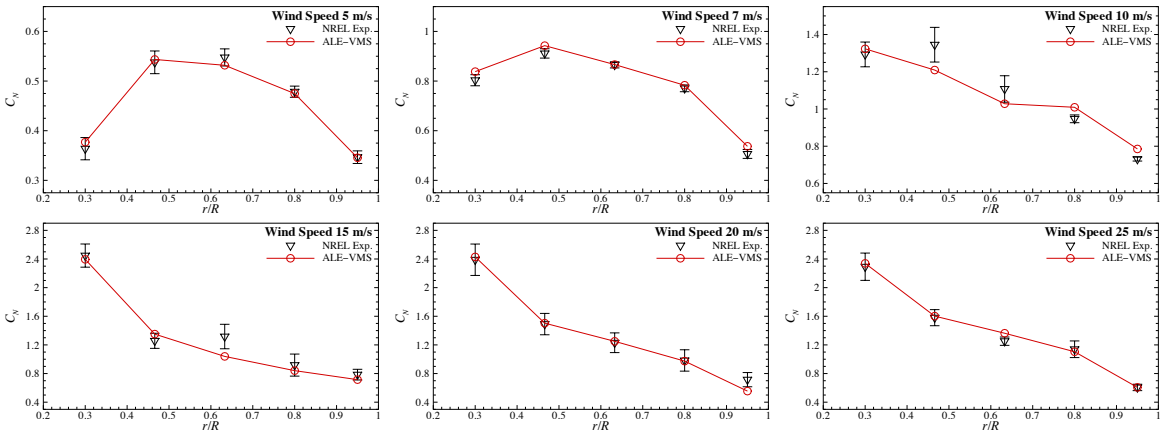

Figure 7. Normal force coefficient at five spanwise stations for different wind speeds. Plus and minus one standard deviation is shown for the NREL experimental data.

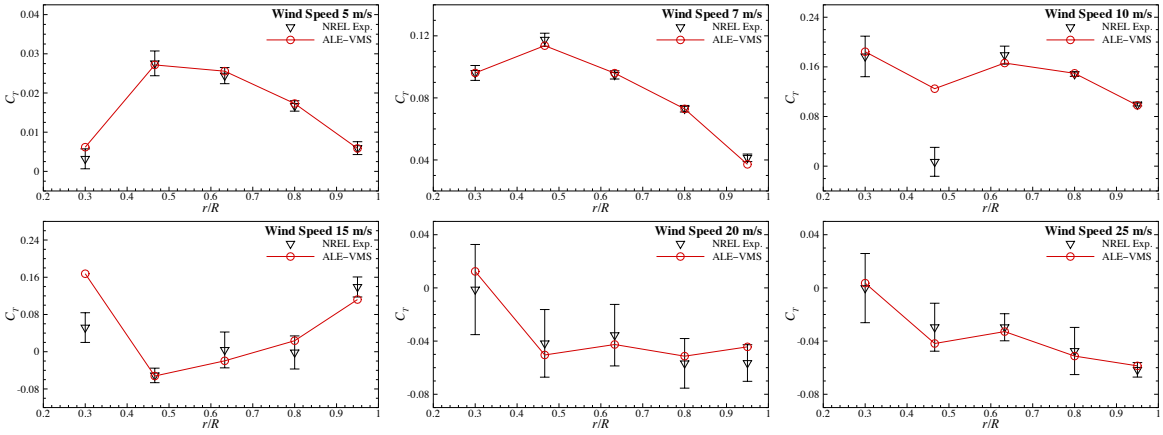

Figure 8. Tangential force coefficient at five spanwise stations for different wind speeds. Plus and minus one standard deviation is shown for the NREL experimental data.

Air speed contours and velocity streamlines at $r/R = 80\%$ are shown in Figure 4 for all cases. The flow is fully attached for the 5 to 10 m/s cases, and is separated for the 15 to 25 m/s cases. The 20 and 25 m/s cases are under heavily stalled

Wind Energ. 2012; **00**:1–20 © 2012 John Wiley & Sons, Ltd.
DOI: 10.1002/we
Prepared using weauth.cls

conditions and the flow separates at the leading edge. The flow separation occurs due to the increased angle of attack created by the increased wind speed relative to the constant rotational speed. The pressure contours at $r/R = 80\%$ are shown in Figure 5 for all cases. The differences in the pressure contours between the attached and separated flow regimes are evident in the figure.

Time-averaged low-speed shaft (aerodynamic) torque and root flap bending moment are shown in Figure 6 for all wind speeds. Overall, the simulation results and experimental data match remarkably well. Although, there is a slight under-prediction of the aerodynamic torque for the high wind speed cases, and a slight over-predictions of the root flap bending moment for the low wind speed cases.

Figures 7 and 8 show the normal and tangential force coefficients, respectively, at five spanwise stations for the wind speeds considered. The force coefficient is an integration of pressure limited to a spanwise station of the blade. Good agreement with experimental data is generally found. The computed force coefficients mostly fall within one standard deviation of the experimental data. Exceptions are found for 10 and 15 m/s wind speeds at some spanwise stations.

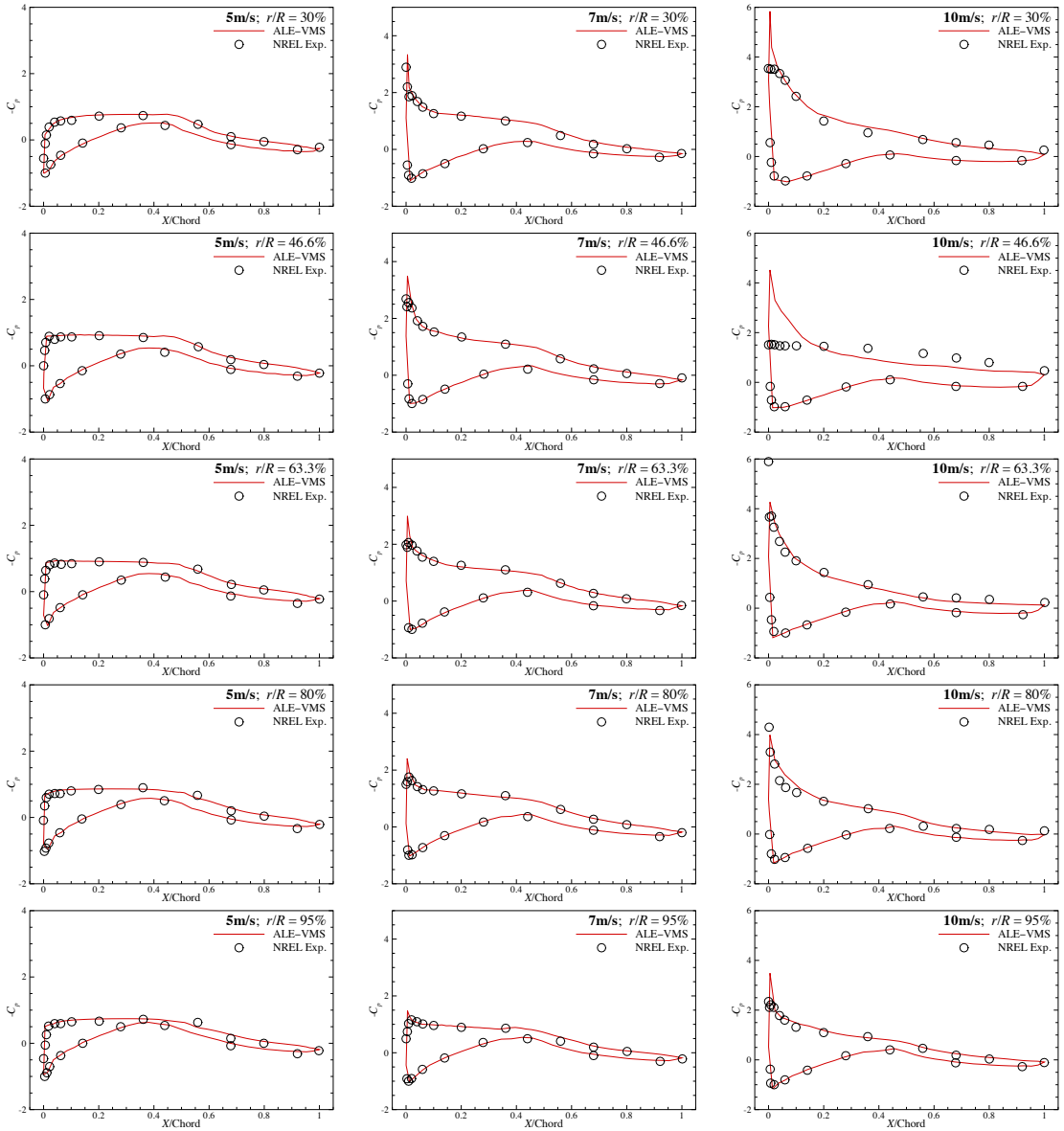

Figure 9. Pressure coefficient at 30%, 46.6%, 63.3%, 80% and 95% spanwise stations for 5, 7, and 10 m/s cases. The predicted values are plotted with the experimental data.

The low-speed shaft torque, root flap bending moment, and force coefficients represent the integrated effect of the aerodynamic loads acting on the rotor blades. It is also of interest to assess the local flow behavior by examining a distribution of the pressure coefficient over the blade surface. The sectional pressure coefficient C_p is computed using the following expression

$$C_p = \frac{p - p_\infty}{\frac{1}{2}\rho\left(U^2 + (r\omega)^2\right)},$$

where U is the inflow wind speed, and ω is the rotor speed. Figures 9 and 10 show the pressure coefficient at 30%, 46.6%, 63.3%, 80% and 95% spanwise stations of the blade for all wind speeds considered. The predicted values are plotted together with the experimental data. While most of the simulation results compare very well against experimental data at different radial locations, notable differences are found for 10 m/s wind speed at location $r/R = 46.6\%$, and for 15 m/s wind speed at location $r/R = 30\%$. However, as shown in Figure 11, for these two wind speed cases, similar discrepancies were found in the computational results of other researchers [1, 2, 10]. As a result, we conducted a mesh refinement study

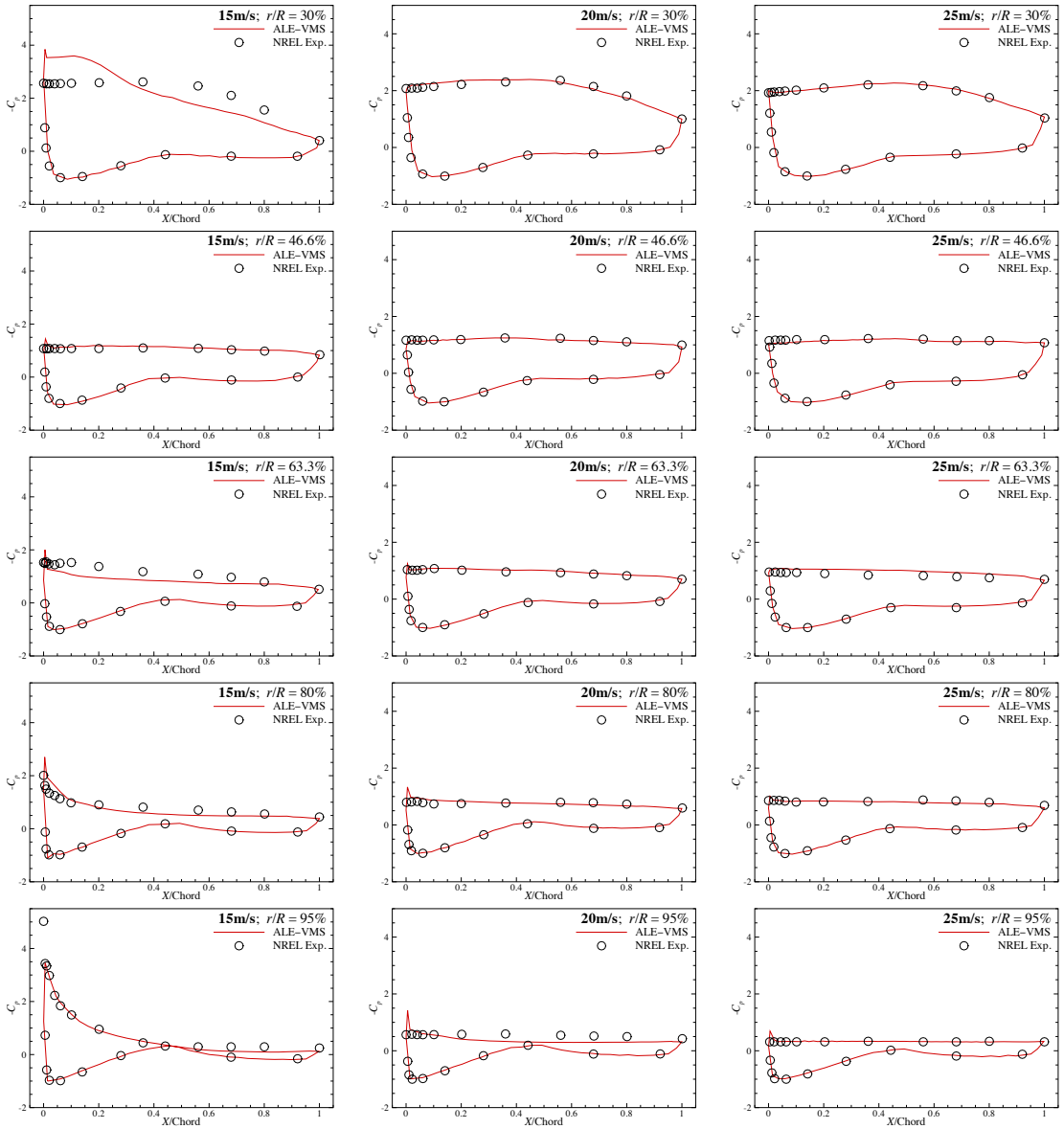

Figure 10. Pressure coefficient at 30%, 46.6%, 63.3%, 80% and 95% spanwise stations for 15, 20, and 25 m/s cases. The predicted values are plotted with the experimental data.

Wind Energ. 2012; **00**:1–20 © 2012 John Wiley & Sons, Ltd.
DOI: 10.1002/we
Prepared using weauth.cls

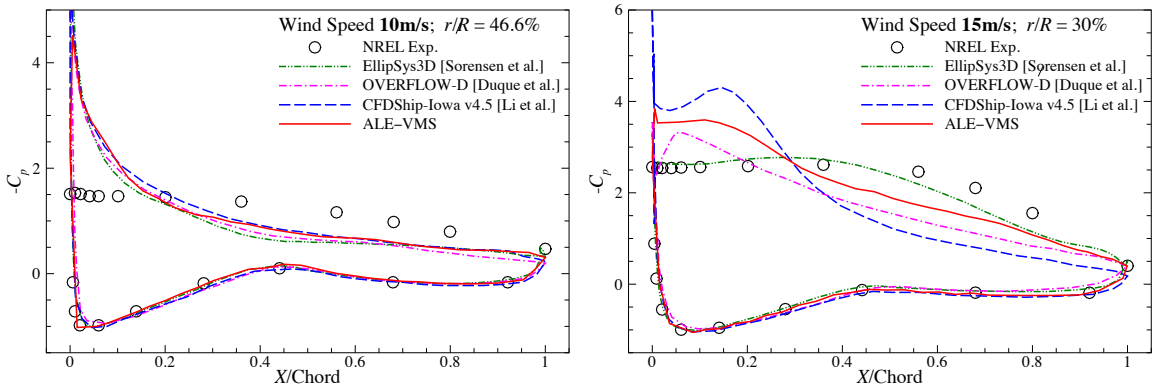

Figure 11. Pressure coefficient for 10 m/s wind speed at location $r/R = 46.6\%$ and 15 m/s wind speed at location $r/R = 30\%$. The ALE–VMS results are compared with the experimental data and computational results of other researchers [1, 2, 10].

for the 10 m/s wind speed case to see if the discrepancies are due to the lack of sufficient mesh resolution. This study is presented in the next section.

Remark 4. Note that the same finite element ALE–VMS formulation given by Eq. (4) is employed to compute the entire range of wind speeds. The numerical results show that the formulation automatically adapts to, and accurately captures a full range of flow regimes present in this application, from the laminar and attached flow, to the turbulent and separated flow. There is no need to select an "appropriate turbulence model" for a given flow regime to better match the experimental data. This feature underscores the predictive capability of the finite element ALE–VMS method for this class of problems, as well as other applications.

3.2. Mesh refinement study

To show the convergence of the ALE–VMS method, a refinement study based on three different meshes was carried out for the 10 m/s wind case. The mesh size on the surface of the rotor and the bounding box that encloses the rotor was reduced

Table II. Mesh statistics for the refinement study. The mesh size on the surface of the rotor and the bounding box that encloses the rotor was reduced by a factor of $\sqrt{2}$ with each refinement.

	Number of Nodes	Number of Elements
Mesh 1	583,627	1,991,891
Mesh 2	1,126,615	3,795,447
Mesh 3	2,178,147	7,328,867

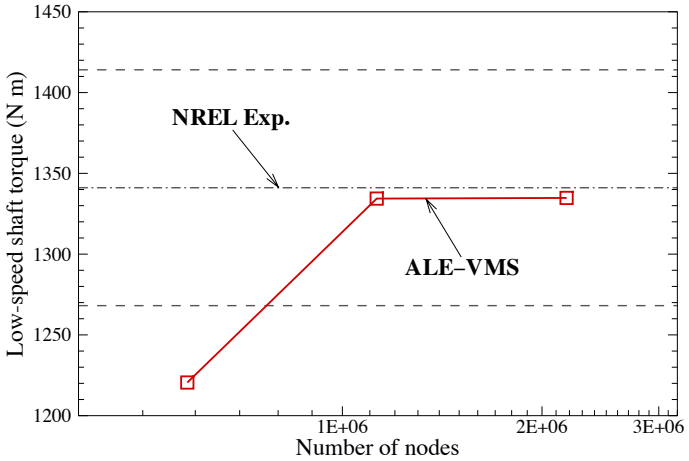

Figure 12. The aerodynamic torque for the 10 m/s case. The results show convergence with mesh refinement.

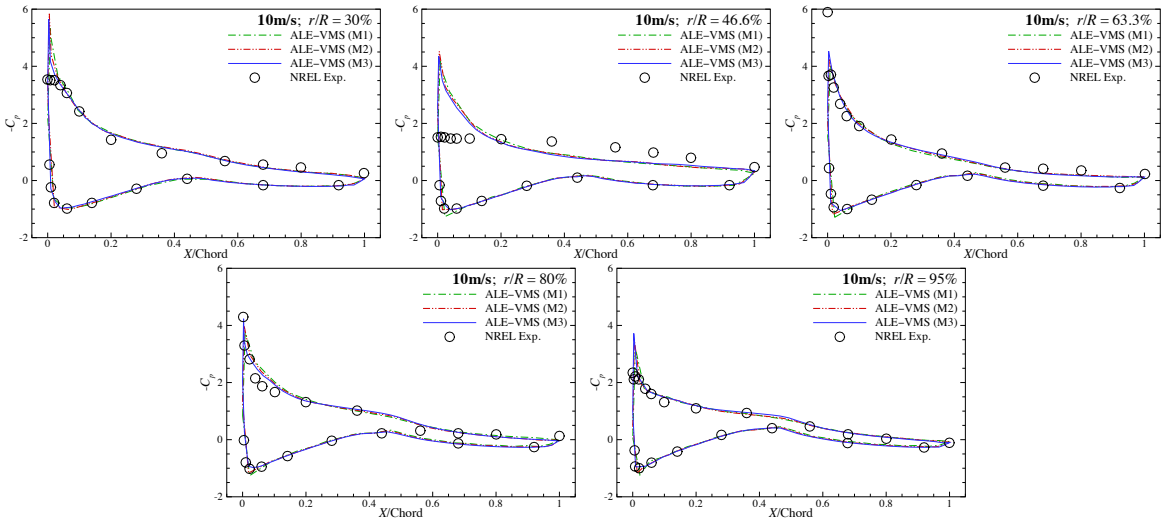

Figure 13. Pressure coefficient at different spanwise stations for the 10 m/s case. The results show convergence with mesh refinement.

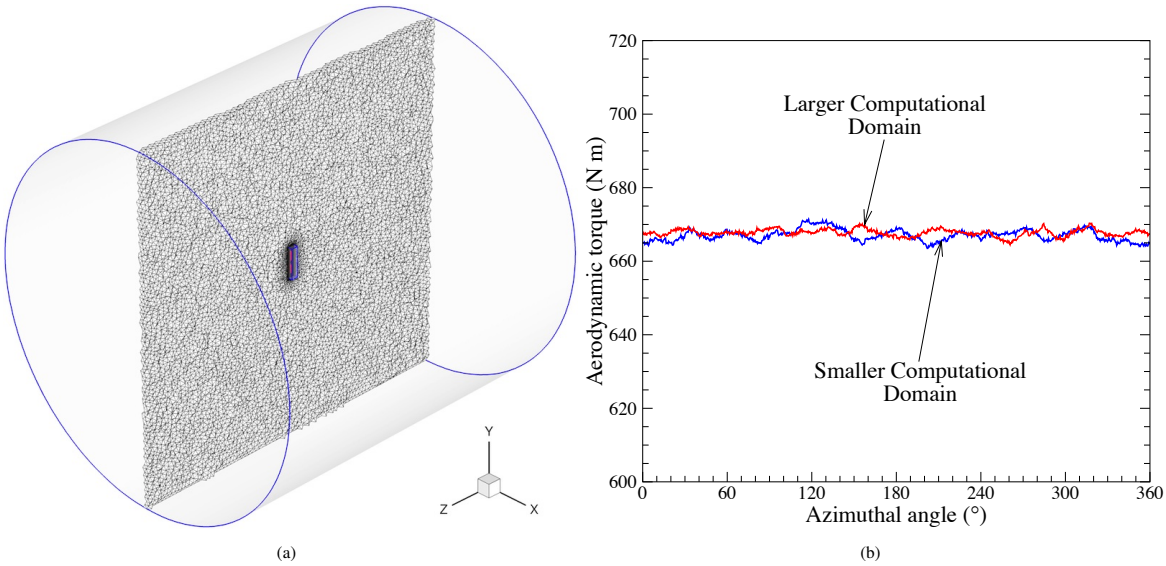

Figure 14. Larger-domain computation. (a) Domain and mesh. The cylindrical domain has the diameter and height of $16D$, where D is the rotor diameter. (b) Comparison of the aerodynamic torque results for smaller and larger computational domains.

by a factor of $\sqrt{2}$ with each refinement. The mesh statistics are summarized in Table II. We note that Mesh 2 was used for all computations in the previous section. Figures 12 and 13 show the results for the aerodynamic torque and pressure coefficient, respectively. Convergence under mesh refinement is achieved for both quantities. Note that the discrepancy between the computational results and experimental data at location $r/R = 46.6\%$ is still present.

3.3. Larger-domain computation

Finally, we investigate the effect of the placement of the outer domain boundaries on the computational results. Figure 14(a) shows the new setup where the domain is $8D$ in all directions. Here D is the rotor diameter. Because $8D$ is measured from the center of the rotor, the cylindrical domain has the diameter and height of $16D$. The mesh is composed of 7,914,449 linear elements and 1,840,069 nodes. As shown in Figure 14(b), the aerodynamic torques computed using larger and smaller computational domains are very close. The results indicate that the smaller domain size chosen for all computations in the previous sections is adequate for this wind turbine rotor.

Wind Energ. 2012; **00**:1–20 © 2012 John Wiley & Sons, Ltd.
DOI: 10.1002/we
Prepared using weauth.cls

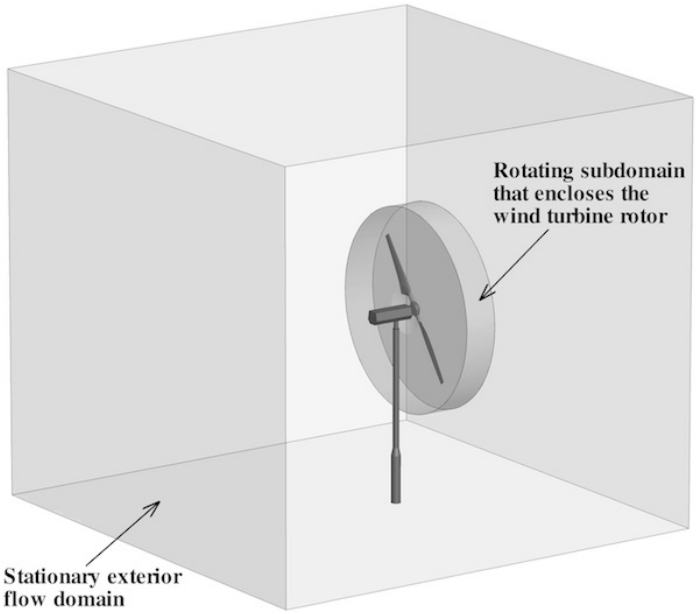

Figure 15. Setup for a full-wind-turbine simulation. An interior rotating subdomain, which encloses the wind-turbine rotor, and an exterior stationary subdomain, which houses the nacelle and tower, are employed.

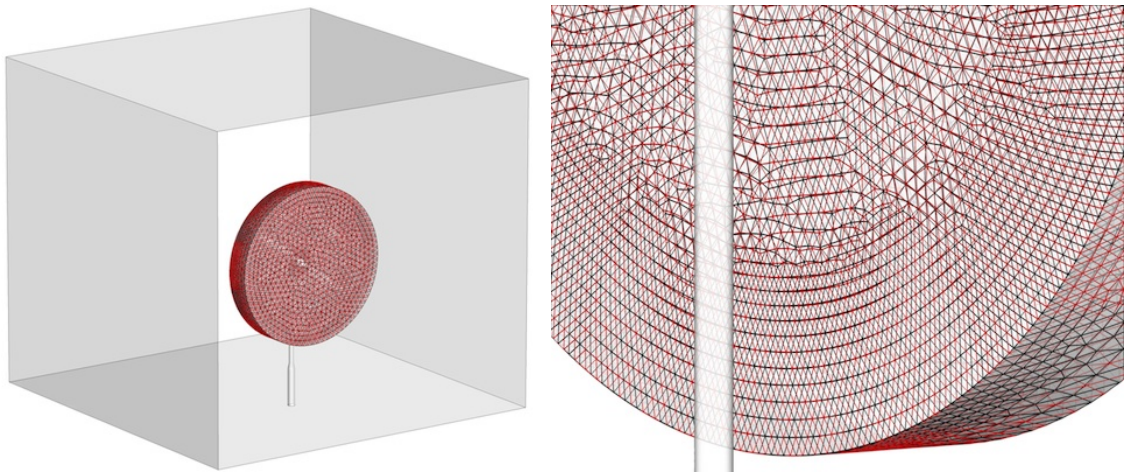

Figure 16. Non-matching meshes at the sliding interface between the stationary and rotating subdomains.

4. SIMULATION OF THE FULL WIND TURBINE

The results presented so far were rotor-only computations, where the wind turbine rotor is housed in a cylindrical domain and the rotation is applied to the entire computational domain. However, to simulate the full wind turbine configuration and investigate the blade–tower interaction, this approach is no longer suitable. Instead, we consider an approach that makes use of a rotating subdomain, which encloses the entire wind turbine rotor, and a stationary subdomain that contains the rest of the wind turbine (see Figure 15). The two domains are in relative motion and share a sliding cylindrical interface. Because of the relative motion, the meshes on each side of the interface are non-matching (see Figure 16). As a result, a numerical procedure is needed that imposes the continuity of the kinematic and traction fields despite the fact that the interface discretizations of the stationary and rotating subdomains are incompatible. Such a procedure is presented in what follows.

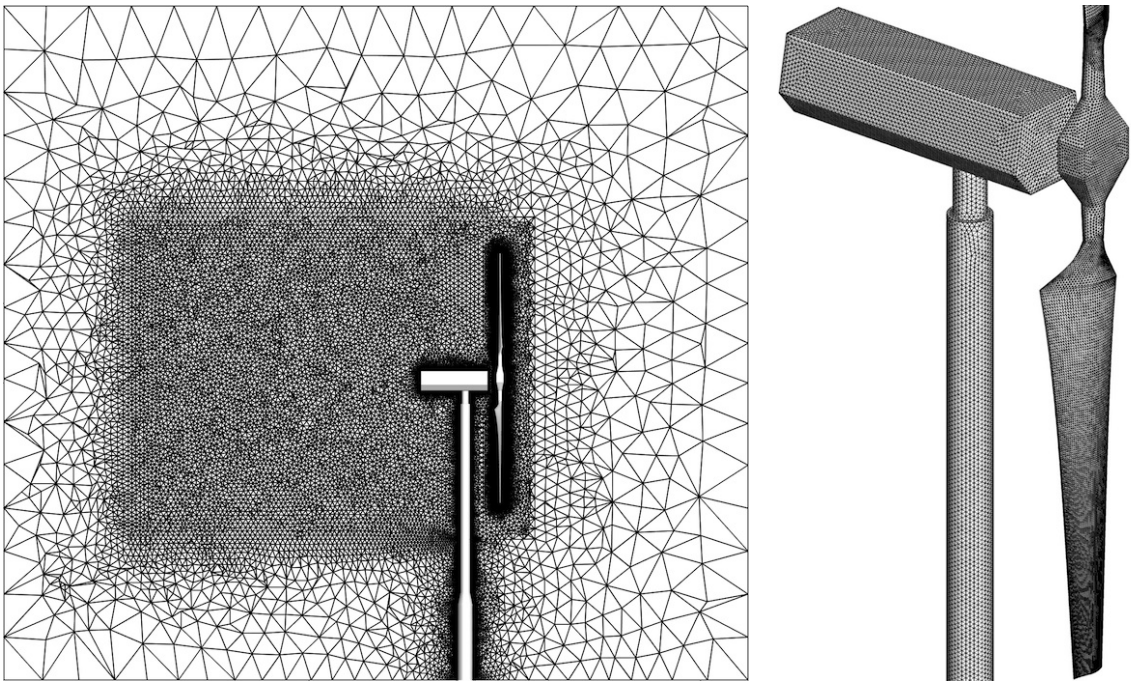

Figure 17. Meshes used in the full-wind-turbine simulation. Left: A 2D cut at $x = 0$ to show the flow domain mesh quality. Right: Surface meshes on rotor, nacelle and tower.

4.1. The sliding-interface formulation

The sliding-interface formulation presented here was first proposed by Bazilevs and Hughes [31] in the context of Isogeometric Analysis (IGA) [23] of flows about rotating components. The advantage of IGA for rotating-component flows is that the cylindrical sliding interfaces are represented exactly, and no geometry errors are incurred. In the case of standard FEM, the geometric compatibility is only approximate.

Let subscripts 1 and 2 denote the quantities pertaining to the fluid mechanics problem on the stationary and rotating subdomains, respectively. The semi-discrete formulation that weakly imposes the continuity of the fluid velocity and traction vectors at the sliding interface is stated as: find $\{\mathbf{u}_1^h, p_1^h\}$ and $\{\mathbf{u}_2^h, p_2^h\}$, such that $\forall\{\mathbf{w}_1^h, q_1^h\}$ and $\{\mathbf{w}_2^h, q_2^h\}$

$$
\begin{aligned}
&B_1^{VW}(\{\mathbf{w}_1^h, q_1^h\}, \{\mathbf{u}_1^h, p_1^h\}; \hat{\mathbf{u}}_1^h) - F_1(\{\mathbf{w}_1^h, q_1^h\}) + B_2^{VW}(\{\mathbf{w}_2^h, q_2^h\}, \{\mathbf{u}_2^h, p_2^h\}; \hat{\mathbf{u}}_2^h) - F_2(\{\mathbf{w}_2^h, q_2^h\}) \\
&- \sum_{b=1}^{N_{\text{eb}}} \int_{\Gamma_t^b \cap (\Gamma_t)_{\text{I}}} \left(\mathbf{w}_1^h - \mathbf{w}_2^h\right) \cdot \frac{1}{2} \left(\boldsymbol{\sigma}_1\left(\mathbf{u}_1^h, p_1^h\right)\mathbf{n}_1 - \boldsymbol{\sigma}_2\left(\mathbf{u}_2^h, p_2^h\right)\mathbf{n}_2\right) \, \mathrm{d}\Gamma \\
&- \sum_{b=1}^{N_{\text{eb}}} \int_{\Gamma_t^b \cap (\Gamma_t)_{\text{I}}} \frac{1}{2} \left(\delta\boldsymbol{\sigma}_1\left(\mathbf{w}_1^h, q_1^h\right)\mathbf{n}_1 - \delta\boldsymbol{\sigma}_2\left(\mathbf{w}_2^h, q_2^h\right)\mathbf{n}_2\right) \cdot \left(\mathbf{u}_1^h - \mathbf{u}_2^h\right) \, \mathrm{d}\Gamma \\
&- \sum_{b=1}^{N_{\text{eb}}} \int_{\Gamma_t^b \cap (\Gamma_t)_{\text{I}}} \mathbf{w}_1^h \cdot \rho \left\{\left(\mathbf{u}_1^h - \hat{\mathbf{u}}_1^h\right) \cdot \mathbf{n}_1\right\}_- \left(\mathbf{u}_1^h - \mathbf{u}_2^h\right) \, \mathrm{d}\Gamma \\
&- \sum_{b=1}^{N_{\text{eb}}} \int_{\Gamma_t^b \cap (\Gamma_t)_{\text{I}}} \mathbf{w}_2^h \cdot \rho \left\{\left(\mathbf{u}_2^h - \hat{\mathbf{u}}_2^h\right) \cdot \mathbf{n}_2\right\}_- \left(\mathbf{u}_2^h - \mathbf{u}_1^h\right) \, \mathrm{d}\Gamma \\
&+ \sum_{b=1}^{N_{\text{eb}}} \int_{\Gamma_t^b \cap (\Gamma_t)_{\text{I}}} \frac{C_I^B \mu}{h_n} \left(\mathbf{w}_1^h - \mathbf{w}_2^h\right) \cdot \left(\mathbf{u}_2^h - \mathbf{u}_1^h\right) \, \mathrm{d}\Gamma = 0,
\end{aligned}
\tag{17}
$$

where

$$
B^{VW}(\{\mathbf{w}^h, q^h\}, \{\mathbf{u}^h, p^h\}; \hat{\mathbf{u}}^h) = B^{VMS}(\{\mathbf{w}^h, q^h\}, \{\mathbf{u}^h, p^h\}; \hat{\mathbf{u}}^h) + B^{WBC}(\{\mathbf{w}^h, q^h\}, \{\mathbf{u}^h, p^h\}; \hat{\mathbf{u}}^h), \tag{18}
$$

and

$$
\delta\boldsymbol{\sigma}\left(\mathbf{w}^h, q^h\right) = q^h\mathbf{I} + 2\mu\boldsymbol{\varepsilon}\left(\mathbf{w}^h\right). \tag{19}
$$

The terms on the first line of Eq. (17) correspond to the ALE–VMS formulation with weak boundary conditions in the stationary and rotating subdomains. The rest of the terms in Eq. (17) are associated with the weak enforcement of the kinematic and traction compatibility at the sliding interface. Here, $(\Gamma_t)_1$ denotes the interface between the stationary and rotating subdomains, and $\{\mathcal{A}\}_-$ denotes the negative part of $\mathcal{A}$, that is, $\{\mathcal{A}\}_- = \mathcal{A}$ if $\mathcal{A} < 0$ and $\{\mathcal{A}\}_- = 0$ if $\mathcal{A} \geq 0$. The formulation may be seen as a Discontinuous Galerkin method (see, e.g., Arnold *et al.* [69]), where the continuity of the basis function is enforced everywhere in the interior of the two subdomains, but not at the sliding interface between them. The structure of the terms on the sliding interface is similar to that of the weak enforcement of essential boundary conditions (see Eq. (6)). The significance of each term is explained in detail in Bazilevs and Hughes [31]. Note that, in this case, $\hat{\mathbf{u}}_1^h = \mathbf{0}$, because domain 1 is stationary. However, the formulation is able to handle situations where both subdomains 1 and 2 are in motion.

4.2. Simulation results

The sliding-interface formulation is applied to the simulation of the full NREL Phase VI wind turbine configuration, including the rotor (blades and hub), nacelle and tower. The tower is composed of two cylinders with diameters of 0.6096 m and 0.4064 m that are connected with a short conical section. The tower height is 11.144 m above the wind tunnel floor. The detailed geometry and configuration of the tower and nacelle can be found in Hand *et al.* [29]. In this study, we considered 7 and 10 m/s wind speed cases from the same experimental sequence S mentioned in Section 3.1. Figure 17 shows the mesh quality and resolution used in the full-wind-turbine computation. The mesh is highly refined near the rotor, nacelle and tower, as well as downstream of the wind turbine to better capture the wake turbulence. The mesh is comprised of 6,835,647 linear elements and 1,603,377 nodes. The time step size, outflow boundary conditions, air density and viscosity, and the details of boundary-layer meshing are the same as in Section 3.1. The slip condition is set on the top, bottom and lateral boundaries. At the inflow boundary the wind speed is set to 7 or 10 m/s.

Figures 18 and 19 show the flow visualization of the full-wind-turbine simulations of the 7 and 10 m/s cases, respectively. The flow structures are different between the two cases. The tip vortex for the 7 m/s case decays very slowly as it is convected downstream, while the tip vortex breaks down quickly for the 10 m/s case. Figure 20 shows the flow field when the blade passes in front of the tower for the 7 m/s case. Note that no visible discontinuities are seen in the flow field at the sliding interface, which indicates that the method correctly handles the kinematic compatibility in this location.

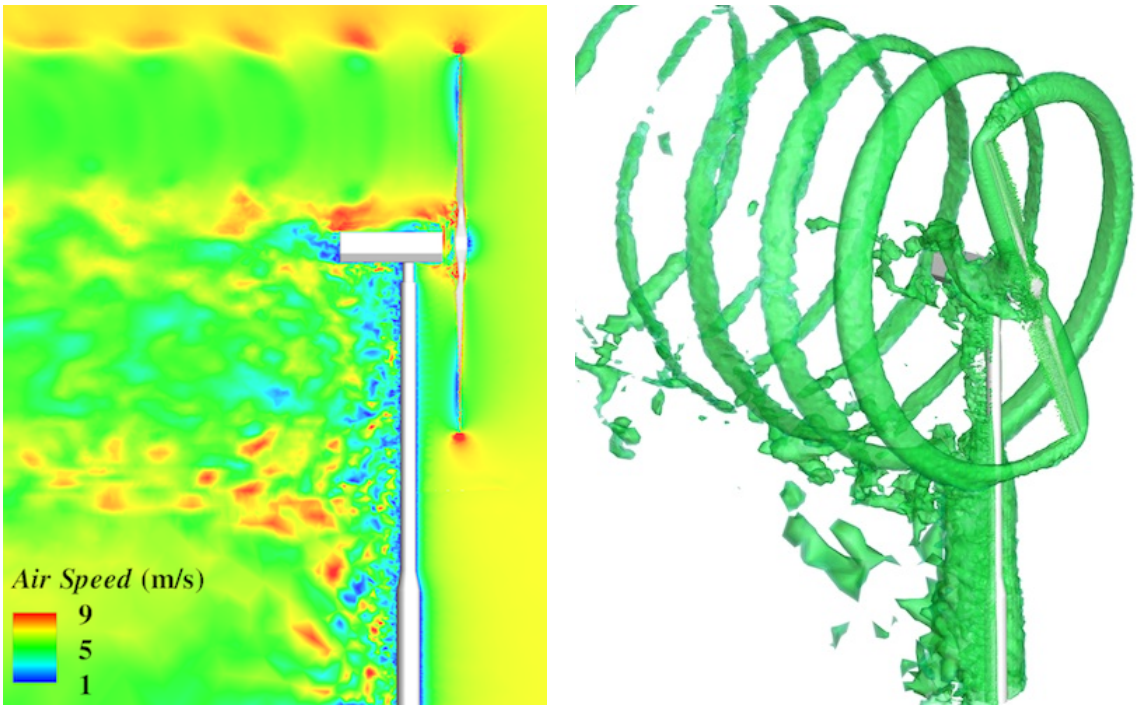

Figure 18. Air speed contours at a planar cut (left), and isosurfaces of air speed (right) at an instant for the 7 m/s case.

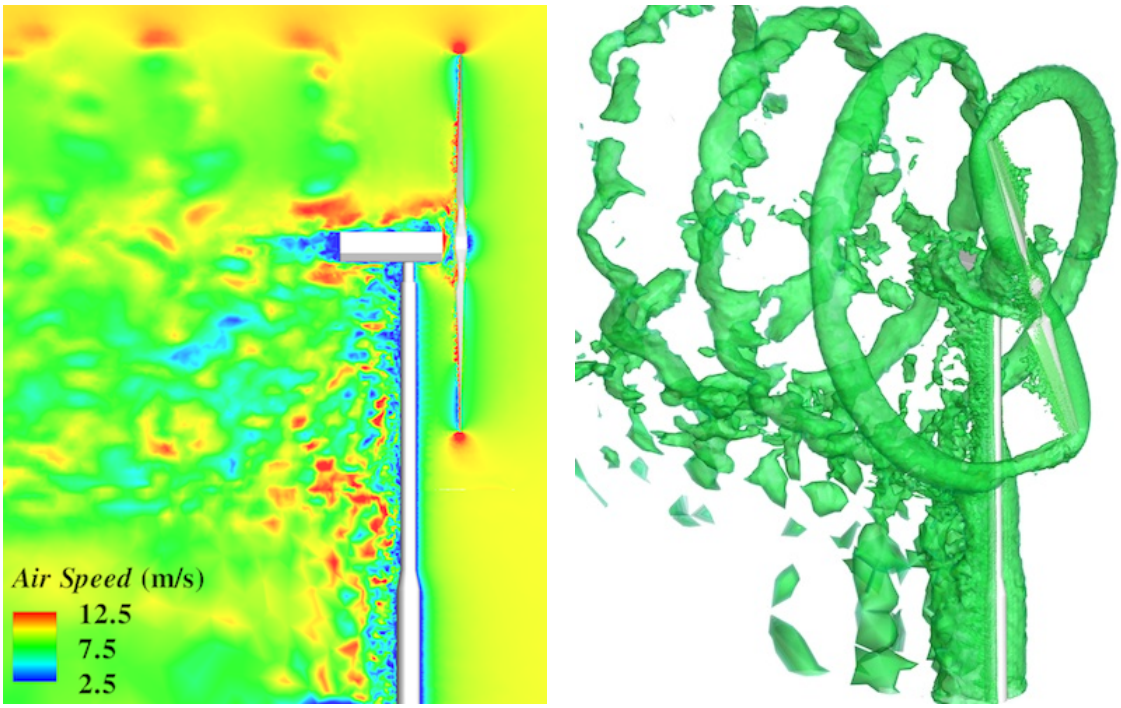

Figure 19. Air speed contours at a planar cut (left), and isosurfaces of air speed (right) at an instant for the 10 m/s case.

To see the influence of the tower, the single-blade aerodynamic torque over a full revolution is plotted in Figure 21 for both 7 and 10 m/s cases. The results of the full-wind-turbine computations are compared with the experimental data[†], as well as with the results of the rotor-only computations.

For the full-wind-turbine simulation of the 7 m/s case, Figure 21(a) clearly shows the drop in the aerodynamic torque at an instant when the blade passes in front of the tower, which corresponds to the azimuthal angle of 180°. The drop in the torque is about 8% relative to its value when the blade is away from the tower. These results are in good agreement with the experimental data. The rotor-only computation is obviously unable to predict this feature, which may be important for the transient structural response of the blades (not considered in this work). It should be noted, however, that the cycle-averaged aerodynamic torque is nearly identical for the full-wind-turbine and the rotor-only simulations. The picture is completely different for the 10 m/s case, where the influence of the tower, although clearly present, is a lot less pronounced.

5. CONCLUSIONS

In this study we applied the ALE–VMS finite element formulation of aerodynamics to the simulation of wind turbines at full scale. The methodology was validated using the NREL Phase VI wind turbine for which there is an extensive set of experimental results. We found that the combination of ALE–VMS method and weakly enforced boundary conditions is able to accurately predict the key quantities of engineering interest such as the aerodynamic torque and pressure distribution at the blade cross-sections. It should be noted that in all cases the same discrete formulation was employed.

It appears that independent of the flow conditions (turbulent, laminar, fully attached, partially attached, fully detached, etc.), the proposed ALE–VMS formulation with weakly enforced no-slip boundary conditions is able to predict the flow solution correctly. This is typically not the case for classical turbulence models, which need to be adjusted for every flow regime separately.

[†]The experimental data plotted in Figure 21 corresponds to the "estimated aerodynamic torque" data adjusted to match the mean of the "corrected low-speed shaft torque" data. The former is obtained by integrating the experimental pressure measurements along the span of the blade, while the latter is obtained from strain-gauge data corrected to remove the gravity effect. Because only five span-wise cross-sections were employed in the calculation of the "estimated aerodynamic torque", we feel that the mean value produced by the strain-gauge measurement is more reliable. On the other hand, because the gravity effect is removed in an approximate manner, we feel that the fluctuating component of the data is more accurately captured using span-wise pressure integration. For more discussion on this see Hand *et al.* [29].

Wind Energ. 2012; **00**:1–20 © 2012 John Wiley & Sons, Ltd.
DOI: 10.1002/we
Prepared using weauth.cls

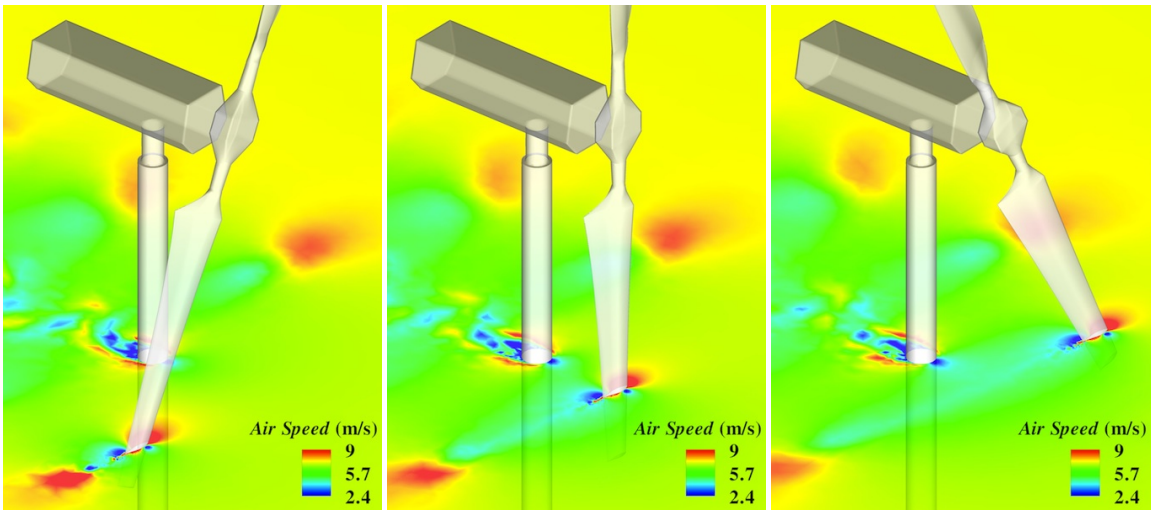

Figure 20. Air speed contours at 80% spanwise station for the 7 m/s case.

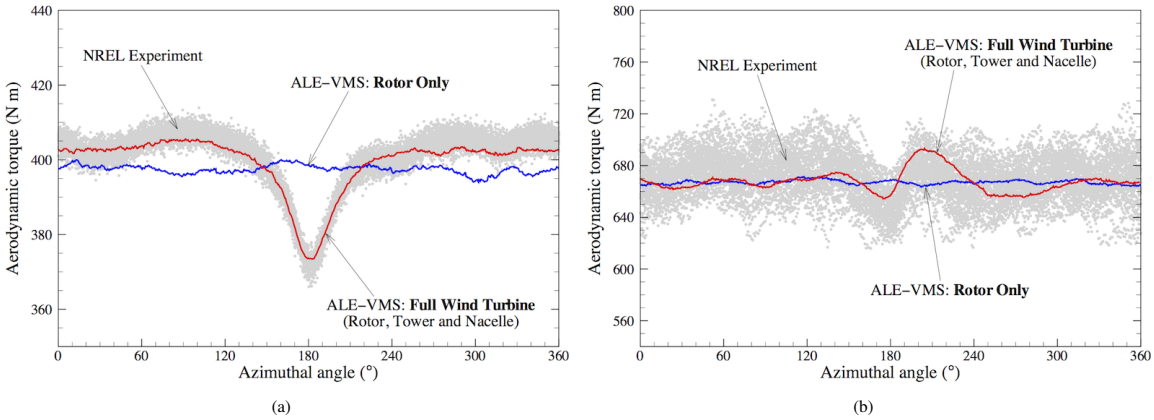

Figure 21. The single-blade aerodynamic torque over a full revolution for (a) 7 m/s and (b) 10 m/s cases. The 180° azimuthal angle corresponds to the instant when the blade passes in front the tower. The tower effect is clearly pronounced in the 7 m/s case. It is also present in the 10 m/s case, but is not as significant. The results in both cases are in very good agreement with the experimental data.

The rotor–tower interaction was handled using a sliding-interface technique. The influence of the tower was correctly captured in the aerodynamic loads, where appreciable differences between the full-wind-turbine and rotor-only simulations were observed. The simulation results for the blade–tower interaction cases are also in very good agreement with the experimental data.

We feel that the rotor-only computations are reasonably accurate for predicting the mean aerodynamic performance of the wind turbine rotors. However, the presence of the tower has an appreciable effect for the dynamic blade loading, which may be important when considering structural analysis of wind turbine blades, or coupled FSI. The tower effects may be even more pronounced for large rotors, which are used in offshore environments, as well as in the cases of low blade-tower clearance and downwind rotor configurations. We plan to look at these cases in the future.

The use of the ALE formulation for wind turbine aerodynamics may be seen as an alternative technique to using an aerodynamics formulation in the rotating frame of reference. We find the use of ALE helpful in the context of the sliding-interface technique to describe rotor–tower interaction, although a technique based on using two frames of reference, one rotating and one stationary, may also be successfully employed. However, when it comes to FSI coupling with flexible turbine blades, the ALE framework is significantly simpler to use than a framework based on a rotating reference frame. For a recent article, which reports on the full-wind-turbine (full-machine) FSI simulation of the NREL 5 MW wind turbine, see Hsu and Bazilevs [70].

ACKNOWLEDGEMENTS

The support of the NSF CAREER Award No. 1055091 and the AFOSR Award No. FA9550-12-1-0005 are gratefully acknowledged. M.-C. Hsu was partially supported by the Los Alamos–UC San Diego Educational Collaboration Fellowship. We thank the Texas Advanced Computing Center (TACC) at the University of Texas at Austin for providing HPC resources that have contributed to the research results reported in this paper. We would also like to acknowledge Dr. Scott Schreck at the National Renewable Energy Laboratory (NREL) for providing the NREL UAE Phase VI data.

REFERENCES

1. Sørensen NN, Michelsen JA, Schreck S. Navier–Stokes predictions of the NREL Phase VI rotor in the NASA Ames 80 ft × 120 ft wind tunnel. *Wind Energy* 2002; **5**:151–169.
2. Duque EPN, Burklund MD, Johnson W. Navier–Stokes and comprehensive analysis performance predictions of the NREL Phase VI experiment. *Journal of Solar Energy Engineering* 2003; **125**:457–467.
3. Le Pape A, Lecanu J. 3D Navier–Stokes computations of a stall-regulated wind turbine. *Wind Energy* 2004; **7**:309–324.
4. Chao DD, van Dam CP. Computational aerodynamic analysis of a blunt trailing-edge airfoil modification to the NREL Phase VI rotor. *Wind Energy* 2007; **10**:529–550.
5. Gómez-Iradi S, Steijl R, Barakos GN. Development and validation of a CFD technique for the aerodynamic analysis of HAWT. *Journal of Solar Energy Engineering* 2009; **131**:031 009–1–13.
6. Zahle F, Sørensen NN, Johansen J. Wind turbine rotor-tower interaction using an incompressible overset grid method. *Wind Energy* 2009; **12**:594–619.
7. Bazilevs Y, Hsu MC, Akkerman I, Wright S, Takizawa K, Henicke B, Spielman T, Tezduyar TE. 3D simulation of wind turbine rotors at full scale. Part I: Geometry modeling and aerodynamics. *International Journal for Numerical Methods in Fluids* 2011; **65**:207–235.
8. Takizawa K, Henicke B, Tezduyar TE, Hsu MC, Bazilevs Y. Stabilized space-time computation of wind-turbine rotor aerodynamics. *Computational Mechanics* 2011; **48**:333–344.
9. Bechmann A, Sørensen NN, Zahle F. CFD simulations of the MEXICO rotor. *Wind Energy* 2011; **14**:677–689.
10. Li Y, Paik KJ, Xing T, Carrica PM. Dynamic overset CFD simulations of wind turbine aerodynamics. *Renewable Energy* 2012; **37**:285–298.
11. Sørensen NN, Schreck S. Computation of the National Renewable Energy Laboratory Phase-VI rotor in pitch motion during standstill. *Wind Energy* 2012; doi:10.1002/we.480.
12. Scheurich F, Brown RE. Modelling the aerodynamics of vertical-axis wind turbines in unsteady wind conditions. *Wind Energy* 2012; doi:10.1002/we.532.
13. Chow R, van Dam CP. Verification of computational simulations of the NREL 5 MW rotor with a focus on inboard flow separation. *Wind Energy* 2012; doi:10.1002/we.529.
14. Kong C, Bang J, Sugiyama Y. Structural investigation of composite wind turbine blade considering various load cases and fatigue life. *Energy* 2005; **30**:2101–2114.
15. Lund E, Stegmann J. On structural optimization of composite shell structures using a discrete constitutive parametrization. *Wind Energy* 2005; **8**:109–124.
16. Hansen MOL, Sørensen JN, Voutsinas S, Sørensen N, Madsen HA. State of the art in wind turbine aerodynamics and aeroelasticity. *Progress in Aerospace Sciences* 2006; **42**:285–330.
17. Jensen FM, Falzon BG, Ankersen J, Stang H. Structural testing and numerical simulation of a 34 m composite wind turbine blade. *Composite Structures* 2006; **76**:52–61.
18. Kiendl J, Bazilevs Y, Hsu MC, Wüchner R, Bletzinger KU. The bending strip method for isogeometric analysis of Kirchhoff–Love shell structures comprised of multiple patches. *Computer Methods in Applied Mechanics and Engineering* 2010; **199**:2403–2416.
19. Bazilevs Y, Hsu MC, Kiendl J, Benson DJ. A computational procedure for pre-bending of wind turbine blades. *International Journal for Numerical Methods in Engineering* 2012; **89**:323–336.
20. Cárdenas D, Escárpita AA, Elizalde H, Aguirre JJ, H Ahuett PM, Probst O. Numerical validation of a finite element thin-walled beam model of a composite wind turbine blade. *Wind Energy* 2012; **15**:203–223.
21. Bazilevs Y, Hsu MC, Kiendl J, Wüchner R, Bletzinger KU. 3D simulation of wind turbine rotors at full scale. Part II: Fluid–structure interaction modeling with composite blades. *International Journal for Numerical Methods in Fluids* 2011; **65**:236–253.
22. Takizawa K, Henicke B, Montes D, Tezduyar TE, Hsu MC, Bazilevs Y. Numerical-performance studies for the stabilized space-time computation of wind-turbine rotor aerodynamics. *Computational Mechanics* 2011; **48**:647–657.

23. Hughes TJR, Cottrell JA, Bazilevs Y. Isogeometric analysis: CAD, finite elements, NURBS, exact geometry and mesh refinement. *Computer Methods in Applied Mechanics and Engineering* 2005; **194**:4135–4195.
24. Cottrell JA, Hughes TJR, Bazilevs Y. *Isogeometric Analysis: Toward Integration of CAD and FEA*. Wiley: Chichester, 2009.
25. Bazilevs Y, Calo VM, Cottrel JA, Hughes TJR, Reali A, Scovazzi G. Variational multiscale residual-based turbulence modeling for large eddy simulation of incompressible flows. *Computer Methods in Applied Mechanics and Engineering* 2007; **197**:173–201.
26. Bazilevs Y, Michler C, Calo VM, Hughes TJR. Weak Dirichlet boundary conditions for wall-bounded turbulent flows. *Computer Methods in Applied Mechanics and Engineering* 2007; **196**:4853–4862.
27. Bazilevs Y, Michler C, Calo VM, Hughes TJR. Isogeometric variational multiscale modeling of wall-bounded turbulent flows with weakly enforced boundary conditions on unstretched meshes. *Computer Methods in Applied Mechanics and Engineering* 2010; **199**:780–790.
28. Bazilevs Y, Akkerman I. Large eddy simulation of turbulent Taylor–Couette flow using isogeometric analysis and the residual–based variational multiscale method. *Journal of Computational Physics* 2010; **229**:3402–3414.
29. Hand MM, Simms DA, Fingersh LJ, Jager DW, Cotrell JR, Schreck S, Larwood SM. Unsteady aerodynamics experiment phase VI: Wind tunnel test configurations and available data campaigns 2001. Technical Report NREL/TP-500-29955, National Renewable Energy Laboratory, Golden, CO.
30. Simms D, Schreck S, Hand M, Fingersh LJ. NREL unsteady aerodynamics experiment in the NASA–Ames wind tunnel: A comparison of predictions to measurements 2001. Technical Report NREL/TP-500-29494, National Renewable Energy Laboratory, Golden, CO.
31. Bazilevs Y, Hughes TJR. NURBS-based isogeometric analysis for the computation of flows about rotating components. *Computatonal Mechanics* 2008; **43**:143–150.
32. Tezduyar T, Aliabadi S, Behr M, Johnson A, Kalro V, Litke M. Flow simulation and high performance computing. *Computational Mechanics* 1996; **18**:397–412.
33. Behr M, Tezduyar T. The Shear-Slip Mesh Update Method. *Computer Methods in Applied Mechanics and Engineering* 1999; **174**:261–274.
34. Behr M, Tezduyar T. Shear-slip mesh update in 3D computation of complex flow problems with rotating mechanical components. *Computer Methods in Applied Mechanics and Engineering* 2001; **190**:3189–3200.
35. Bazilevs Y, Hughes TJR. Weak imposition of Dirichlet boundary conditions in fluid mechanics. *Computers & Fluids* 2007; **36**:12–26.
36. Hughes TJR, Liu WK, Zimmermann TK. Lagrangian–Eulerian finite element formulation for incompressible viscous flows. *Computer Methods in Applied Mechanics and Engineering* 1981; **29**:329–349.
37. Johnson C. *Numerical solution of partial differential equations by the finite element method*. Cambridge University Press: Sweden, 1987.
38. Brenner SC, Scott LR. *The Mathematical Theory of Finite Element Methods, 2nd ed.* Springer, 2002.
39. Ern A, Guermond JL. *Theory and Practice of Finite Elements*. Springer, 2004.
40. Brooks AN, Hughes TJR. Streamline upwind/Petrov–Galerkin formulations for convection dominated flows with particular emphasis on the incompressible Navier–Stokes equations. *Computer Methods in Applied Mechanics and Engineering* 1982; **32**:199–259.
41. Hughes TJR, Tezduyar TE. Finite element methods for first-order hyperbolic systems with particular emphasis on the compressible Euler equations. *Computer Methods in Applied Mechanics and Engineering* 1984; **45**:217–284.
42. Tezduyar TE, Park YJ. Discontinuity capturing finite element formulations for nonlinear convection-diffusion-reaction equations. *Computer Methods in Applied Mechanics and Engineering* 1986; **59**:307–325.
43. Hughes TJR, Franca LP, Balestra M. A new finite element formulation for computational fluid dynamics: V. Circumventing the Babuška–Brezzi condition: A stable Petrov–Galerkin formulation of the Stokes problem accommodating equal-order interpolations. *Computer Methods in Applied Mechanics and Engineering* 1986; **59**:85–99.
44. Tezduyar TE, Osawa Y. Finite element stabilization parameters computed from element matrices and vectors. *Computer Methods in Applied Mechanics and Engineering* 2000; **190**:411–430.
45. Tezduyar TE. Computation of moving boundaries and interfaces and stabilization parameters. *International Journal for Numerical Methods in Fluids* 2003; **43**:555–575.
46. Hughes TJR, Scovazzi G, Franca LP. Multiscale and stabilized methods. *Encyclopedia of Computational Mechanics, Vol. 3, Fluids*, Stein E, de Borst R, Hughes TJR (eds.). chap. 2, Wiley, 2004.
47. Bazilevs Y, Calo VM, Hughes TJR, Zhang Y. Isogeometric fluid–structure interaction: theory, algorithms, and computations. *Computational Mechanics* 2008; **43**:3–37.
48. Hsu MC, Bazilevs Y, Calo VM, Tezduyar TE, Hughes TJR. Improving stability of stabilized and multiscale formulations in flow simulations at small time steps. *Computer Methods in Applied Mechanics and Engineering* 2010; **199**:828–840.

49. Hughes TJR. Multiscale phenomena: Green's functions, the Dirichlet-to-Neumann formulation, subgrid scale models, bubbles, and the origins of stabilized methods. *Computer Methods in Applied Mechanics and Engineering* 1995; **127**:387–401.
50. Hughes TJR, Feijóo GR, Mazzei L, Quincy JB. The variational multiscale method–A paradigm for computational mechanics. *Computer Methods in Applied Mechanics and Engineering* 1998; **166**:3–24.
51. Hughes TJR, Sangalli G. Variational multiscale analysis: the fine-scale Green's function, projection, optimization, localization, and stabilized methods. *SIAM Journal of Numerical Analysis* 2007; **45**:539–557.
52. Takizawa K, Tezduyar TE. Multiscale space–time fluid–structure interaction techniques 2011. Computational Mechanics.
53. Hsu MC, Akkerman I, Bazilevs Y. Wind turbine aerodynamics using ALE–VMS: validation and the role of weakly enforced boundary conditions. *Computational Mechanics* 2012; **50**:499–511.
54. Jonkman JM. Modeling of the UAE wind turbine for refinement of FAST_AD 2003. Technical Report NREL/TP-500-34755, National Renewable Energy Laboratory, Golden, CO.
55. Johansen J, Sørensen NN, Michelsen JA, Schreck S. Detached-eddy simulation of flow around the NREL Phase VI blade. *Wind Energy* 2002; **5**:185–197.
56. Laino DJ, Hansen AC, Minnema JE. Validation of the AeroDyn subroutines using NREL Unsteady Aerodynamics Experiment data. *Wind Energy* 2002; **5**:227–244.
57. Tongchitpakdee C, Benjanirat S, Sankar LN. Numerical simulation of the aerodynamics of horizontal axis wind turbines under yawed flow conditions. *Journal of Solar Energy Engineering* 2005; **127**:464–474.
58. Sezer-Uzol N, Long LN. 3-D time-accurate CFD simulations of wind turbine rotor flow fields 2006. AIAA Paper 2006-0394.
59. Schmitz S, Chattot JJ. Characterization of three-dimensional effects for the rotating and parked NREL Phase VI wind turbine. *Journal of Solar Energy Engineering* 2006; **128**:445–454.
60. Huang JC, Lin H, Hsieh TJ, Hsieh TY. Parallel preconditioned WENO scheme for three-dimensional flow simulation of NREL Phase VI rotor. *Computers & Fluids* 2011; **45**:276–282.
61. Somers DM. Design and experimental results for the S809 airfoil 1997. Technical Report NREL/SR-440-6918, National Renewable Energy Laboratory, Golden, CO.
62. Texas Advanced Computing Center (TACC). Available at: http://www.tacc.utexas.edu. Accessed 25 March 2012.
63. Karypis G, Kumar V. A fast and high quality multilevel scheme for partitioning irregular graphs. *SIAM Journal on Scientific Computing* 1999; **20**:359–392.
64. Hsu MC, Akkerman I, Bazilevs Y. High-performance computing of wind turbine aerodynamics using isogeometric analysis. *Computers & Fluids* 2011; **49**:93–100.
65. Chung J, Hulbert GM. A time integration algorithm for structural dynamics with improved numerical dissipation: The generalized-α method. *Journal of Applied Mechanics* 1993; **60**:371–75.
66. Jansen KE, Whiting CH, Hulbert GM. A generalized-α method for integrating the filtered Navier-Stokes equations with a stabilized finite element method. *Computer Methods in Applied Mechanics and Engineering* 2000; **190**:305–319.
67. Saad Y, Schultz MH. GMRES: A generalized minimal residual algorithm for solving nonsymmetric linear systems. *SIAM Journal of Scientific and Statistical Computing* 1986; **7**:856–869.
68. Shakib F, Hughes TJR, Johan Z. A multi-element group preconditioned GMRES algorithm for nonsymmetric systems arising in finite element analysis. *Computer Methods in Applied Mechanics and Engineering* 1989; **75**:415–456.
69. Arnold DN, Brezzi F, Cockburn B, Marini LD. Unified analysis of Discontinuous Galerkin methods for elliptic problems. *SIAM Journal of Numerical Analysis* 2002; **39**:1749–1779.
70. Hsu MC, Bazilevs Y. Fluid–structure interaction modeling of wind turbines: simulating the full machine. *Computational Mechanics* 2012; doi:10.1007/s00466-012-0772-0.

Wind Energ. 2012; **00**:1–20 © 2012 John Wiley & Sons, Ltd.
DOI: 10.1002/we
Prepared using weauth.cls